Research Square

Preprints are preliminary reports that have not undergone peer review.
They should not be considered conclusive, used to inform clinical practice,
or referenced by the media as validated information.

Mechanisms of Dissimilarity in Turbulent Transport of Momentum and Heat in the Vegetation Roughness Sublayer

Sagufta Tarannum
Northeastern University
Khaled Ghannam
k.ghannam@northeastern.edu
Northeastern University

Research Article

Keywords:

Posted Date: November 19th, 2026

DOI: https://doi.org/10.21203/rs.3.rs-11661577/v1

License: This work is licensed under a Creative Commons Attribution 4.0 International License.
Read Full License

Additional Declarations: No competing interests reported.

Noname manuscript No.
(will be inserted by the editor)

Mechanisms of Dissimilarity in Turbulent Transport of Momentum and Heat in the Vegetation Roughness Sublayer

Sagufta Tarannum · Khaled Ghannam

Received: DD Month YEAR / Accepted: DD Month YEAR

Abstract

This paper presents an observational analysis of the kinematic and dynamical mechanisms underlying the dissimilarity in turbulent transport of momentum and heat fluxes in the vegetation roughness sublayer (RSL). Using eddy-covariance measurements above a tall Amazon forest canopy, the results show that the transport efficiency (correlation coefficient) of momentum is higher than that of heat even under near-neutral conditions, in contrast to the traditional assumption of a similar momentum–scalar transport in this regime. Quadrant analysis reveals that the reduced efficiency of momentum transport under both unstable and stable conditions is driven by a weakening of downgradient fluxes (primarily sweep events) and strengthening of countergradient interactions, while the increased efficiency of heat under unstable conditions is mostly driven by strengthening of ejections within buoyant plumes. Besides bulk transport efficiencies, lagged cross-correlations indicate that small-scale eddies in the inertial subrange have negligible contribution to net momentum transport, but otherwise actively transport heat fluxes across all stability regimes. Consequently, momentum exchange occurs through larger, more organized motions that exhibit longer decorrelation timescales (eddy lifetimes) than heat-carrying eddies in the RSL. An analysis of the steady-state flux budgets links this contrast in eddy lifetimes to the pressure-scrambling mechanisms that act as the primary sink for both fluxes, where flux relaxation timescales estimated through a Rotta closure closely follow the observed decorrelation timescales and suggest that pressure–temperature-gradient interactions decor-

S. Tarannum
Department of Civil and Environmental Engineering, Northeastern University, Boston, MA

K. Ghannam
Department of Civil and Environmental Engineering, Northeastern University, Boston, MA
E-mail: k.ghannam@northeastern.edu

relate the heat flux more rapidly than pressure–strain interactions destroy momentum flux.

Keywords Canopy turbulence · Coherent structures · Flux budgets · Momentum–heat dissimilarity · Roughness sublayer

1 Introduction

Airflow within and above vegetation canopies plays a central role in the turbulent exchange of momentum, heat, and mass between the land surface and the atmospheric boundary layer (ABL). Compared to canonical rough-wall boundary layer flows, tall vegetation canopies extend into what would otherwise be the inertial sublayer of the ABL, such that the vertically distributed drag exerted by plant elements on the flow and the active source-sink distribution of heat and other scalars (e.g., CO_2, water vapor) remain dynamically relevant to turbulent transport processes above the canopy (Harman and Finnigan 2007; Bonan et al. 2018; Ghannam et al. 2020; Zahn et al. 2022). This coupling between the canopy sublayer (CSL)—the airspace between the ground surface and the canopy top—and the roughness sublayer (RSL)—the region extending from the canopy top to few canopy heights—gives rise to a complex phenomenology of turbulence where transport mechanisms are governed by the interplay among canopy drag, shear instabilities associated with strong mean velocity gradients near the canopy top, and thermal stratification of the ABL (Finnigan 2000; Cava and Katul 2012; Dupont and Patton 2012b; Chowdhuri et al. 2022). While this conceptualization of canopy flows is well established (Finnigan et al. 2009; Brunet 2020), an outstanding challenge toward their improved parameterization concerns the contrasting behavior of momentum and heat transport, often referred to as momentum–heat dissimilarity. Such contrast represents a departure from the Reynolds analogy, which posits that momentum and heat are transported by the same turbulent eddies with comparable efficiency. Understanding the physical mechanisms underlying this dissimilarity has important implications on the representation of canopy turbulence in numerical models, including the parameterization of the turbulent Prandtl number (Li 2019).

Since the early works of Wilczak (1984) and Katul and Parlange (1994), momentum–heat transport dissimilarity has been shown to be intrinsically linked to the role of buoyancy in modifying the structure and organization of coherent turbulent motions responsible for vertical transport (Li and Bou-Zeid 2011; Dupont and Patton 2012b; Lan et al. 2022). Under near-neutral stratification, where coherent motions are predominantly shear-driven, the temperature field behaves approximately as a passive scalar such that momentum and heat have comparable transport efficiencies. In contrast, under unstable stratification, the active role of temperature in buoyancy production of turbulent kinetic energy promotes the formation of thermal/convective plumes that preferentially enhance heat transport relative to momentum, leading to a breakdown of the Reynolds analogy (Katul et al. 1997; Li and Bou-Zeid 2011).

The topology of these coherent structures has been widely studied through conditional sampling (quadrant analysis) (e.g., Raupach 1981; Poggi et al. 2004; Chowdhuri and Prabha 2019), particularly in the analysis of momentum transport (Shaw et al. 1983; Katul et al. 2006; Poggi and Katul 2007; Finnigan et al. 2009). Both field and laboratory experiments of canopy flows show that coherent structures organize RSL turbulence into ejection–sweep cycles that dominate momentum transport (cf. a review by Brunet 2020). Such cycles are characterized by intermittent, high-amplitude sweeps ($w' < 0$ and $u' > 0$; i.e., downdrafts carrying high-momentum air) that ventilate the canopy airspace, and quiescent ejections ($w' > 0$ and $u' < 0$) that represent updrafts of low-momentum air. Here, u' and w' are turbulent fluctuations in the longitudinal (streamwise) and vertical (wall-normal) velocity components, respectively, such that $\overline{u'w'}$ is the vertical kinematic momentum flux (Reynolds stress), and the overline symbol denotes Reynolds/time averaging. Quadrant analysis has also been applied to heat fluxes ($\overline{w'T'}$) following similar conditional-sampling principles, and measurements across a range of surface topographies indicate that buoyancy forces enhance heat transport by strengthening the coupling between vertical velocity (w') and temperature (T') fluctuations, while simultaneously decorrelating w' and u' fluctuations, thereby reducing the transport efficiency of momentum relative to heat (Katul et al. 1997; Christen et al. 2007; Ghannam et al. 2017). However, the specific mechanisms (ejections and sweeps) that underpin these buoyancy-induced changes to flux transport efficiencies remain poorly constrained in canopy flows, especially under stable atmospheric stratification, although the common assumption that the turbulent Prandtl number is unity in such conditions suggests weak dissimilarity (Li 2019).

The interpretation of momentum–heat transport dissimilarity through the stability-dependent coupling between w' fluctuations and their u' or T' counterparts, while phenomenological and kinematic, can be complemented by an analysis of the characteristic timescales governing this coupling to provide further insight into the dynamical mechanisms driving the failure of the Reynolds analogy. Specifically, the present work analyzes the w'-u' and w'-T' coupling through lagged cross-correlations, $\overline{u'(t)w'(t+\tau)}$ and $\overline{T'(t)w'(t+\tau)}$, to extract the decorrelation timescale (τ_d) for each flux, and thereby contrast the lifetime of momentum and heat flux-carrying eddies. Dynamically, τ_d is dictated by the efficiency of the pressure–strain and pressure–temperature-gradient interactions in scrambling the phase relationships between w' and the transported quantity (u' or T') within their respective flux budgets (Katul and Manes 2014; Mortarini et al. 2025; Cava et al. 2006). While these pressure correlations, which act as the main sink terms in the $\overline{u'w'}$ and $\overline{w'T'}$ budgets, are not directly measured in field experiments, a generalized Rotta closure approach can be used to parameterize their slow part in terms of a relaxation timescale (τ_{uw} or τ_{wT}) that characterizes the rate of flux destruction. Estimating these relaxation timescales from the steady-state, horizontally homogeneous flux budgets therefore provides a parallel investigation of the same physical mechanism provided by τ_d. Such a comparison between decorrelation

and relaxation timescales allows the contrast in flux-carrying eddy lifetimes to be examined in the context of the role of pressure-driven flux destruction rates, and hence adds a dynamical context to the kinematic description of momentum–heat dissimilarity.

To investigate the aforementioned arguments, this study uses eddy-covariance measurements from the GoAmazon tower to bridge the kinematic and dynamical interpretations of momentum–heat transport dissimilarity in the vegetation RSL. The analysis focuses on flux transport efficiencies, their decomposition into quadrant contributions, and lagged cross-correlations to characterize how buoyancy modifies the flux decorrelation timescales. The connection to the underlying dynamics is achieved by analyzing the steady-state, horizontally homogeneous flux budgets in the RSL. By employing a Rotta-type relaxation closure, the observed decorrelation timescales are compared to the relaxation timescales inferred from the pressure–strain and pressure–temperature-gradient terms, which are estimated as residuals to the measured budgets. The observational data and theoretical framework are described in Sections 2 and 3, results and discussion are presented in Section 4, and concluding remarks are given in Section 5.

2 Observational data

This section provides an overview of the observational data used in this study and their processing protocol. Throughout, meteorological notation is employed such that the Cartesian coordinates x, y, and z denote the longitudinal (streamwise), lateral (cross-stream), and vertical (wall-normal) directions, respectively, with u, v, and w representing the corresponding velocity components.

2.1 Site description and instrumentation

The work utilizes data from the Green Ocean Amazon (GoAmazon) project (Fuentes et al. 2016; Freire et al. 2017; Gerken et al. 2018; Ghannam et al. 2018). Measurements were collected during a field campaign at the Cuieiras Biological Reserve, located approximately 60 km north-northwest of Manaus, Brazil, between March 2014 and January 2015. The site features a dense primary forest with an average canopy height $h = 35$ m and a leaf area index (LAI) estimated to range from 5.7 to 7.3 $\mathrm{m^2\ m^{-2}}$ (Fuentes et al. 2016). Nine triaxial sonic anemometers (CSAT3; Campbell Scientific) were installed on a 50 m tall tower, providing high-frequency (20 Hz) time series of the three wind velocity components (u, v, w) and sonic virtual temperature (T) within and just above the canopy. The nine measurement heights are $z/h = 0.2$, 0.39, 0.52, 0.63, 0.7, 0.9, 1, 1.15, and 1.38, where z is the height above the ground surface. Much of the analysis in this work is focused on the RSL ($z/h \geq 1$), while measurements in the CSL ($z/h < 1$) are used to characterize vertical mean profiles.

2.2 Data processing and quality control

Turbulent statistics are calculated using a 30-min block averaging period. Each 30-min time series is first despiked using a five-point median filter (Starkenburg et al. 2016), followed by a double coordinate rotation (Kaimal and Finnigan 1994) to align the mean longitudinal velocity ($\overline{u}$) with the x-direction and ensure zero mean lateral and vertical motion ($\overline{v} = \overline{w} = 0$). Turbulent fluctuations (u', v', w', T'), denoted by the prime symbol, are then calculated by removing the linear trend from the corresponding time series. Data blocks that failed the stationarity test proposed by Vickers and Mahrt (1997) were excluded from further analysis, and the mean flow in the RSL is treated as steady ($\partial(.)/\partial t = 0$) and horizontally homogeneous ($\partial(.)/\partial x = \partial(.)/\partial y = 0$). We also exclude time periods where the vertical variations of the fluxes across the three RSL measurement heights were larger than 20%. In total, 393 data blocks are used to analyze the mean statistics and transport efficiencies. However, because the pressure–strain and pressure–temperature-gradient terms are estimated here as residuals to the steady-state, horizontally homogeneous flux budgets (discussed further in Sect. 3), additional quality control is applied to ensure physical consistency, where data blocks are retained only if the mean-gradient production and pressure-correlation terms have opposite signs, consistent with their respective roles as production and sink terms in the budgets. Following this additional screening, 150 of the 190 blocks under unstable conditions are retained, whereas only 64 of the 204 blocks under stable conditions satisfy the criterion. The smaller number of retained blocks under stable conditions is primarily associated with the mean temperature gradient ($\frac{\partial \overline{T}}{\partial z}$), which can change sign across the RSL heights, resulting in a positive mean-gradient production term contrary to its expected sign under stable conditions. These blocks are therefore excluded from both the heat-flux and momentum-flux budgets.

Atmospheric stability of the RSL flow is characterized using the stability parameter, $\zeta = z_d/L$, where $z_d = z - d$ is the height above the zero-plane displacement, $d = 2h/3$, and L is the Obukhov length defined as

$$L = -\frac{u_*^3}{\kappa \beta \overline{w'T'}}, \tag{1}$$

where g is the gravitational acceleration, $\kappa = 0.4$ is the von Kármán constant, and $\beta = g/\overline{T}$ is the buoyancy parameter. Note that T is the sonic virtual temperature, and hence $\overline{w'T'}$ is the kinematic buoyancy flux. The flow regimes are classified as unstable ($z_d/L < -0.1$), near-neutral ($-0.1 \leq z_d/L \leq 0.1$), and stable ($z_d/L > 0.1$). To estimate the vertical gradients $\partial(\cdot)/\partial z$ required for the flux budgets, profiles of the mean variables ($\overline{u}$, $\overline{T}$) and the turbulent transport terms ($\overline{w'u'w'}$, $\overline{w'w'T'}$) are fitted to a second-order polynomial in $\ln(z_d)$ applied over the three measurement heights in the RSL. Finally, the mean flow statistics and flux budgets are normalized using the friction velocity

(u_*) and temperature (T_*) scales,

$$u_* = \sqrt{-\overline{u'w'}}; \qquad T_* = \frac{|\overline{w'T'}|}{u_*}, \tag{2}$$

both evaluated at the canopy top ($z/h = 1$). The momentum flux budget is normalized by $\kappa z_d/u_*^3$, and the heat flux budget by $\kappa z_d/(u_*^2 T_*)$.

3 Theoretical framework

3.1 Flux transport efficiencies and their quadrant decomposition

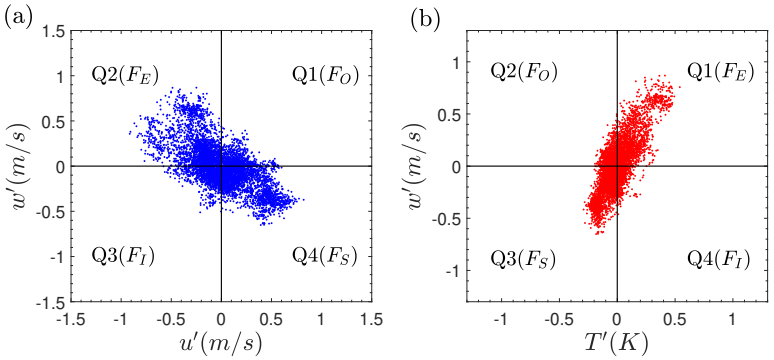


Fig. 1 Definition of the four quadrants used for conditional sampling of the (a) momentum flux and (b) heat flux under unstable stratification. The scatter points illustrate the joint distribution of the turbulent fluctuations from a select 5-minute time series of high-frequency data. Momentum transport is dominated by downgradient fluxes (ejections ≡ Q2 and sweeps ≡ Q4). Heat transport under unstable conditions is dominated by ejections (Q1) and sweeps (Q3), with the remaining quadrants representing countergradient interactions.

The capacity of turbulence to exchange momentum and heat between the canopy and the overlying atmosphere is quantified by the transport efficiency, defined as the correlation coefficient between the vertical velocity and the transported quantity as (e.g., Stull 2012)

$$\gamma_{w\chi} = \frac{\overline{w'\chi'}}{\sigma_w \sigma_\chi}, \tag{3}$$

where σ_w and σ_χ denote the standard deviations of the vertical velocity and the transported variable χ (u or T), respectively. The correlation coefficients γ_{uw} and γ_{wT} are interpreted as transport efficiencies as they represent the ratio of net transport (or "useful work", given by the covariances $\overline{u'w'}$ and $\overline{w'T'}$) to the maximum theoretical transport (or "total effort" given by $\sigma_u \sigma_w$ and $\sigma_w \sigma_T$) (Wyngaard and Moeng 1992).

While the dependence of γ_{uw} and γ_{wT} on RSL stability (z_d/L) is a well-documented feature of momentum–heat dissimilarity (e.g., Li and Bou-Zeid 2011; Lan et al. 2022), the specific transport mechanisms dictating this dependence remain poorly characterized. For instance, it remains unclear whether the reduced efficiency of momentum transport with increasing $|z_d/L|$ is associated with weakening of downgradient fluxes (ejections and/or sweeps) or strengthening of countergradient fluxes (inward and outward interactions). To disentangle these dynamics, the net flux can be partitioned into quadrant contributions using conditional sampling (Raupach 1981; Shaw et al. 1983). Based on the signs of the instantaneous fluctuations, the w'–χ' plane is divided into four quadrants (Q1, Q2, Q3, and Q4, as illustrated in Fig. 1). For momentum transport, the downgradient flux is driven by ejections (Q2: $w' > 0, u' < 0$) and sweeps (Q4: $w' < 0, u' > 0$), while outward (Q1: $w' > 0, u' > 0$) and inward (Q3: $w' < 0, u' < 0$) interactions represent countergradient transport. Heat transport is partitioned in an analogous manner (Katul et al. 1997; Cava et al. 2006), where under unstable conditions (net heat flux is upward), ejections (Q1: $w' > 0, T' > 0$) and sweeps (Q3: $w' < 0, T' < 0$) dominate the transport, while Q2 and Q4 act as countergradient interactions (Fig. 1b). Under stable conditions where $\overline{w'T'} < 0$, the quadrant roles for the heat flux are similar to those of momentum.

The total kinematic flux is the sum (weighted by time fractions) of contributions from the four quadrants, i.e., $\overline{w'\chi'} = F_E + F_S + F_O + F_I$ (Fig. 1), where the subscripts denote ejections, sweeps, outward interactions, and inward interactions, respectively. The bulk transport efficiency can then be decomposed into quadrant-specific efficiencies:

$$\gamma_{w\chi} = \gamma_E + \gamma_S + \gamma_O + \gamma_I = \frac{F_E}{\sigma_w \sigma_\chi} + \frac{F_S}{\sigma_w \sigma_\chi} + \frac{F_O}{\sigma_w \sigma_\chi} + \frac{F_I}{\sigma_w \sigma_\chi}. \tag{4}$$

Decomposing $\gamma_{w\chi}$ following Eq. 4 provides a diagnostic framework to interpret changes to the bulk transport efficiencies (γ_{uw} and γ_{wT}) as a balance between flux-producing transport (γ_E and γ_S) and countergradient interactions (γ_I and γ_O).

3.2 Cross-correlation functions and connections to flux budgets

The quadrant decomposition of transport efficiencies discussed above represents a kinematic description of momentum–heat dissimilarity. To provide a dynamic interpretation, we analyze the lagged cross-correlation functions of momentum and heat fluxes to estimate their decorrelation timescales, and connect their magnitude to the flux destruction mechanisms associated with pressure correlations in the flux budgets. For a stationary process, the normalized lagged cross-correlation function is given as

$$\rho_{\chi w}(\tau) = \frac{\overline{\chi'(t) w'(t+\tau)}}{\overline{\chi' w'}} \tag{5}$$

where τ denotes the time lag, and stationarity implies that $\rho_{\chi w}$ is a function of τ only. By definition, $\rho_{\chi w}(0) = 1$, and the function decays with increasing τ. The flux decorrelation timescale, a characteristic measure of the lifetime of momentum or heat flux-carrying eddies, is estimated as

$$\tau_d = \int_0^\infty \rho_{\chi w}(\tau) d\tau, \tag{6}$$

which is determined here by a trapezoidal integration to estimate the area under the curve of $\rho_{\chi w}(\tau)$. Since the analysis is limited to stationary 30-min data blocks, the integration is performed only up to the first zero crossing of $\rho_{\chi w}(\tau)$.

The decorrelation timescales for momentum $\tau_{d(uw)}$ and heat $\tau_{d(wT)}$ are fundamentally linked to the efficiency of pressure–strain and pressure–temperature-gradient interactions in destroying the $\overline{u'w'}$ and $\overline{w'T'}$ covariances. These interactions represent the main sink terms in their corresponding flux budgets, which for a stationary and horizontally homogeneous flow at high Reynolds number can be written as (Stull 2012):

$$\frac{\partial \overline{u'w'}}{\partial t} \approx 0 = \underbrace{-\overline{w'^2}\frac{\partial \overline{u}}{\partial z}}_{\mathrm{M}_{uw}} - \underbrace{\frac{\partial \left(\overline{w'u'w'}\right)}{\partial z}}_{\mathrm{T}_{uw}} + \underbrace{\frac{g}{\overline{T}}\overline{u'T'}}_{\mathrm{B}_{uw}} + \underbrace{\overline{\frac{1}{\overline{\rho}}p'\left(\frac{\partial u'}{\partial z} + \frac{\partial w'}{\partial x}\right)}}_{\mathrm{R}_{uw}}, \tag{7a}$$

$$\frac{\partial \overline{w'T'}}{\partial t} \approx 0 = \underbrace{-\overline{w'^2}\frac{\partial \overline{T}}{\partial z}}_{\mathrm{M}_{wT}} - \underbrace{\frac{\partial}{\partial z}\left(\overline{w'w'T'}\right)}_{\mathrm{T}_{wT}} + \underbrace{\frac{g}{\overline{T}}\overline{T'^2}}_{\mathrm{B}_{wT}} + \underbrace{\overline{\frac{1}{\overline{\rho}}p'\left(\frac{\partial T'}{\partial z}\right)}}_{\mathrm{R}_{wT}}. \tag{7b}$$

The left hand side of Eqs. 7a and 7b represents the tendency terms $\partial\overline{u'w'}/\partial t = 0$ and $\partial\overline{w'T'}/\partial t = 0$, which vanish for a steady-state flow. The remaining terms correspond to flux production by the mean vertical gradients (M_{uw} and M_{wT}), turbulent transport (T_{uw} and T_{wT}), production or loss of momentum fluxes by the horizontal heat flux (B_{uw}), production or loss of heat fluxes by the temperature variance (B_{wT}), and the pressure-scrambling correlations (R_{uw} and R_{wT}). Note that viscous dissipation is not included in these budgets as it has negligible contribution to flux destruction at high Reynolds numbers in the ABL (Wyngaard et al. 1971; Stull 2012).

The role of pressure correlations as the dominant sink mechanism provides a physical interpretation of the contrast in decorrelation timescales of momentum and heat fluxes. To examine this connection, we calculate R_{uw} and R_{wT} as residuals to the budgets in Eqs. 7a and 7b (all other terms are estimated directly from measurements), and use the generalized Rotta closure model to estimate the relaxation timescale for each flux (Moeng and Wyngaard 1986; Andrén and Moeng 1993; Mironov 2001; Cava et al. 2006; Stull 2012; Ghannam et al. 2017). Specifically, the closure is given by

$$\mathrm{R}_{uw} = \frac{1}{\overline{\rho}}\overline{p'\left(\frac{\partial u'}{\partial z} + \frac{\partial w'}{\partial x}\right)} = -C_1\frac{\overline{u'w'}}{\tau_{uw}} - C_2\frac{g}{\overline{T}}\overline{u'T'} + C_3\overline{w'^2}\frac{\partial \overline{u}}{\partial z}, \tag{8a}$$

$$\mathrm{R}_{wT} = \frac{1}{\overline{\rho}}\overline{p'\left(\frac{\partial T'}{\partial z}\right)} = -C_1\frac{\overline{w'T'}}{\tau_{wT}} - C_2\frac{g}{\overline{T}}\overline{T'^2} + C_3\overline{w'^2}\frac{\partial \overline{T}}{\partial z}. \tag{8b}$$

The first term on the right hand side of Eq. 8 represents the slow part of pressure redistribution (Rotta's model) and is inversely proportional to a relaxation timescale (τ_{uw} or τ_{wT}). This relaxation timescale characterizes the rate at which the pressure-scrambling mechanism decorrelates turbulent fluxes. Importantly, τ_{uw} and τ_{wT} provide a dynamical interpretation of the flux decorrelation timescales τ_d obtained from the lagged cross-correlation analysis as both quantities reflect the same underlying pressure-driven loss of coherence in the flux carrying eddies. The remaining terms in Eq. 8 represent the rapid pressure contributions associated with buoyancy and mean-gradient effects (Mironov 2001). In this study, the model constants are taken as $C_1 = 1.8$, $C_2 = 1/2$, and $C_3 = 2/5$, with C_1 referred to as the Rotta constant (Pope 2001), in agreement with values recommended by previous studies (Katul and Manes 2014; Banerjee et al. 2016; Ghannam et al. 2017; Mortarini et al. 2025).

It is important to note that the estimation of R_{uw} and R_{wT} as residuals to the steady-state and horizontally homogeneous budgets implies that these terms absorb the contributions of processes that are not retained in Eqs. 7a and 7b, such as dispersive fluxes and advection, but also uncertainties in the measured vertical gradients. While this residual approach is common practice for both surface layer and dense canopy flows (Wyngaard et al. 1971; Cava et al. 2006; Ghannam et al. 2017), the terms R_{uw} and R_{wT} are interpreted here as effective pressure correlations, such that the relaxation timescales estimated from the Rotta model are only approximate. Because the work here concerns the relative behavior of momentum and heat, and both residuals are evaluated from the same data blocks under identical assumptions, the errors common to both budgets are expected to influence their contrast less than their individual magnitudes.

4 Results and Discussion

This section presents the main results starting with the bulk flow statistics within and above the canopy, followed by an analysis of the kinematics underlying momentum–heat dissimilarity, and an analysis of the flux budgets to show the role of the pressure scrambling terms R_{uw} and R_{wT} in explaining this dissimilarity.

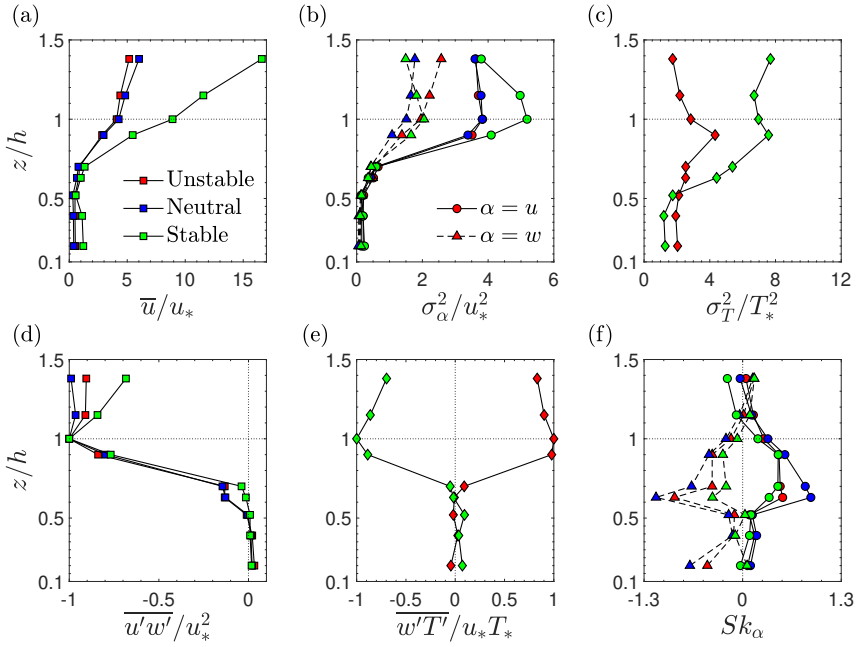


Fig. 2 Ensemble-average profiles of mean-flow and turbulence statistics for (a) mean longitudinal velocity component, (b) velocity variances, (c) temperature variance, (d) momentum flux, (e) heat flux, and (f) velocity skewness. The normalizing scales are the friction velocity u_* and temperature scale T_* at canopy top $z/h = 1$. Results are shown for unstable (red), near-neutral (blue), and stable (green) conditions. In panels (b) and (f), the velocity components u and w are denoted by circle and triangle symbols, respectively. Stability is determined from measurements at the canopy top.

4.1 Bulk Flow Statistics

Figure 2 shows the ensemble-averaged vertical profiles of the mean velocity and turbulence statistics throughout the canopy across neutral, unstable, and stable flow regimes. These profiles are consistent with previous field observations and large-eddy simulations of plant canopies under different stability conditions (Katul and Albertson 1998; Mölder et al. 2004; Launiainen et al. 2007; Dupont and Patton 2012a; Patton et al. 2016; Torkelson et al. 2022). The mean longitudinal wind profile $\overline{u}/u_*$ (Fig. 2a) matches the characteristics typical of dense canopies (Finnigan 2000; Brunet 2020), with a pronounced inflection point near the canopy top associated with sharp velocity gradients due to strong shear in the RSL. The magnitude of $\overline{u}/u_* \approx 4$ at the canopy top under near-neutral conditions (Fig. 2a) is also comparable to wind tunnel data (Macdonald 2000) and large-eddy simulations of canopy flows (Finnigan et al. 2009).

The strong shear and high turbulence intensity in the RSL are also evident in the normalized velocity variances σ_α^2/u_*^2 and momentum flux $\overline{u'w'}/u_*^2$ profiles (Fig. 2b,d), which decay rapidly within the CSL, with most of the momen-

tum being absorbed in the upper half of the canopy. The profile of $\overline{u'w'}/u_*^2$ is largest under near-neutral stratification in the RSL, indicating stronger downward transport of momentum under shear-dominated flow conditions. Another key feature of canopy turbulence is its intermittency which is reflected in the velocity skewness, defined as $Sk_\alpha = \overline{\alpha'^3}/(\sigma_\alpha^2)^{3/2}$, and shown in Fig. 2f. Within the canopy, the combination of strong negative Sk_w and strong positive Sk_u suggests that turbulence is dominated by intermittent but intense downward-moving high-momentum air from above (Finnigan 2000; Dupont and Patton 2012a). This behavior is most pronounced under near-neutral conditions, where skewness attains its highest peak across stability classes, suggesting more organized coherent turbulent motions. The normalized σ_T^2 (Fig. 2c) and $\overline{w'T'}$ (Fig. 2e) both exhibit a rapid increase in the upper canopy due to the dominant heat sources and sinks in this region. In the near-neutral regime, normalized $\overline{w'T'}$ and σ_T^2 are not shown due to non-physical behavior arising from very weak fluxes.

4.2 Coherent structures and flux transport efficiencies in the RSL

To examine how atmospheric stability modulates turbulent transport mechanisms within the RSL, Fig. 3 shows the dependence of the transport efficiencies $|\gamma_{uw}|$ and $|\gamma_{wT}|$ upon z_d/L, along with empirical functions based on Monin-Obukhov similarity theory (MOST) shown as solid lines. These functions are given by (De Bruin et al. 1993; Choi et al. 2004)

$$\gamma_{uw} = \frac{1}{C_{u1}C_{w1}\left(1 - C_{u2}\frac{z_d}{L}\right)^{1/3}\left(1 - C_{w2}\frac{z_d}{L}\right)^{1/3}}, \tag{9a}$$

$$\gamma_{wT} = \frac{\left(1 - C_{T2}\frac{z_d}{L}\right)^{1/3}}{C_{w1}C_{T1}\left(1 - C_{w2}\frac{z_d}{L}\right)^{1/3}}. \tag{9b}$$

where the coefficients used here are $C_{u1} = 2.2$, $C_{u2} = 3$, $C_{w1} = 1.1$, $C_{w2} = 3$, $C_{T1} = 3.3$, and $C_{T2} = 28.4$ (similar to Li and Bou-Zeid 2011). While these formulations were calibrated for atmospheric surface layer (ASL) flows under unstable stratification only, they are used here as a benchmark for comparison between the RSL and the ASL. The curves shown on the stable side of Fig. 3 are obtained by evaluating Eqs. 9a and 9b at $-z_d/L$, so that the unstable regime functions are mirrored about $z_d/L = 0$ with the same coefficients. This is intended to provide a reference to evaluate the trend in transport efficiencies under stable conditions.

While Eqs. 9a and 9b (with the coefficients given above) predict $|\gamma_{uw}| = 0.41$ and $|\gamma_{wT}| = 0.28$ in the neutral limit ($z_d/L \to 0$), the measured efficiencies are $|\gamma_{uw}| \approx 0.5$ (Fig. 3a) and $|\gamma_{wT}| \approx 0.2$ (Fig. 3b), suggesting that momentum transport is somewhat more efficient in the RSL compared to ASL flows, and that the common assumption $|\gamma_{uw}| = |\gamma_{wT}|$ under neutral stratification is

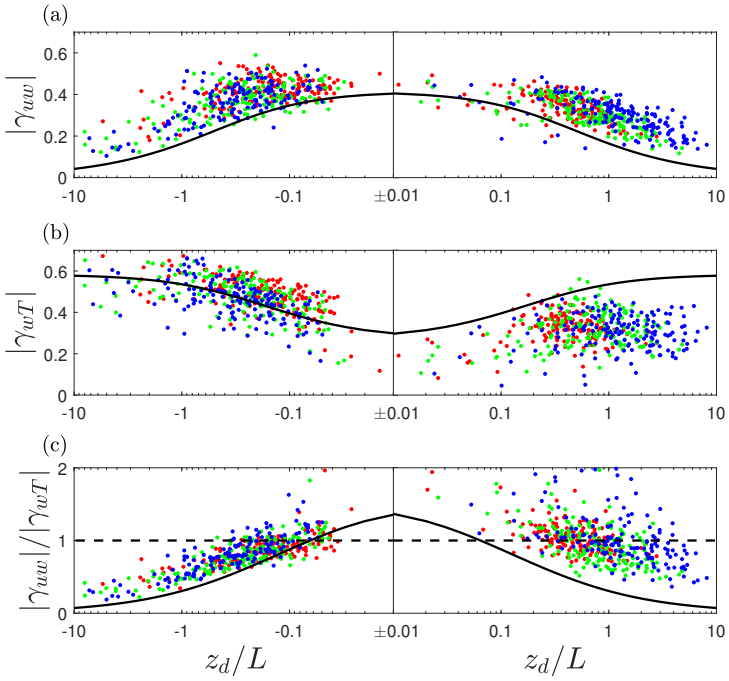


Fig. 3 Absolute values of the transport efficiencies (correlation coefficients) of (a) momentum $|\gamma_{uw}|$, (b) heat $|\gamma_{wT}|$, and (c) their ratio $|\gamma_{uw}|/|\gamma_{wT}|$ within the RSL as a function of the stability parameter z_d/L. The red, green and blue markers correspond to measurements at $z/h = 1$, $z/h = 1.15$, and $z/h = 1.38$, respectively, while the solid black lines denote the empirical formulations (Eqs. 9a and 9b) based on Monin-Obukhov similarity (De Bruin et al. 1993; Li and Bou-Zeid 2011).

not evident in the RSL. Under both unstable and stable conditions, the momentum transport efficiency $|\gamma_{uw}|$ decreases with increasing $|z_d/L|$ (Fig. 3a), largely following the trend of the MOST scaling function, but with consistently higher magnitude throughout the whole $|z_d/L|$ range, further showing that momentum transport remains more efficient in the RSL compared to the ASL predictions given by Eq. 9a. In contrast, heat transport efficiency $|\gamma_{wT}|$ increases with increasing instability ($z_d/L < -0.1$; Fig. 3b), approaching the value $|\gamma_{wT}| = 0.58$ in the free convection limit as predicted by Eq. 9b. Under stable conditions, $|\gamma_{wT}|$ shows no systematic dependence on z_d/L and has pronounced scatter, as well as residing lower than the MOST scaling curve. Consequently, the ratio of momentum to heat transport efficiencies $|\gamma_{uw}|/|\gamma_{wT}|$ decreases with increasing instability (Fig. 3c), indicating that heat transport becomes more efficient than that of momentum for $z_d/L < -0.1$. The ratio $|\gamma_{uw}|/|\gamma_{wT}|$ is more scattered around unity under stable conditions (Fig. 3c), indicating that momentum–heat dissimilarity is less evident when buoyancy acts to suppress turbulent transport.

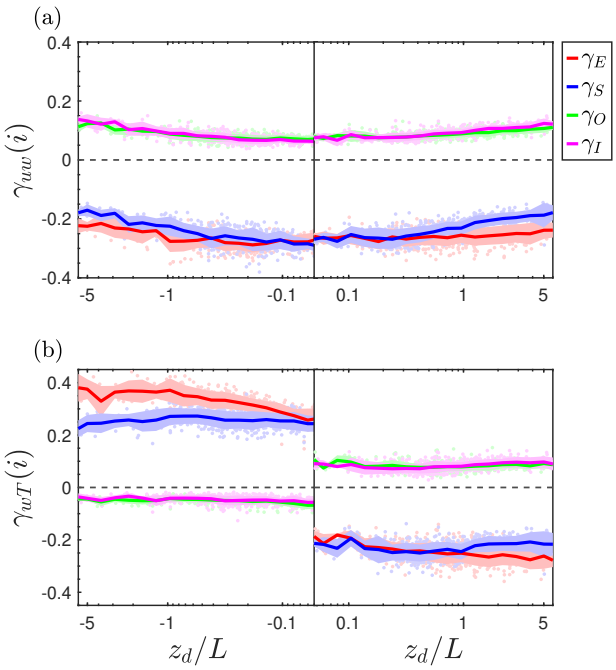


Fig. 4 Decomposition of the transport efficiencies γ_{uw} and γ_{wT} into quadrant contributions associated with ejections (γ_E), sweeps (γ_S), outward (γ_O), and inward (γ_I) interactions for (a) momentum and (b) heat fluxes within the RSL. Solid lines denote the mean, shaded regions indicate $\pm 1\sigma$ (standard deviation), and scattered points represent individual data blocks.

To disentangle how transport by coherent structures shapes the bulk efficiencies discussed above, Fig. 4 shows the decomposition of γ_{uw} and γ_{wT} into quadrant contributions from sweeps (γ_S), ejections (γ_E), and inward (γ_I) and outward (γ_O) interactions following Eq. 4. For momentum (Fig. 4a), the reduced $|\gamma_{uw}|$ is driven by a progressive weakening of the sweep contribution (γ_S) as $|z_d/L|$ increases, accompanied by enhanced countergradient interactions (γ_O and γ_I). The ejection contribution γ_E also weakens with $|z_d/L|$, but to a lesser extent than γ_S (Fig. 4a). This stability dependence of the quadrant contributions indicates that buoyancy effects, under both unstable and stable conditions, weaken the organized and efficient transport of momentum by the ejection–sweep cycle, which is a hallmark of the neutrally stratified shear layer of the RSL (Raupach et al. 1996). A notable aspect of this buoyancy signature is that it is independent of the sign of buoyancy forcing (whether it generates or suppresses turbulence), suggesting that the presence of buoyancy itself weakens the efficient momentum transport by coherent structures in the RSL.

In contrast, the increased transport efficiency of the heat flux $|\gamma_{wT}|$ under unstable conditions is almost entirely driven by enhanced contribution of the

ejection quadrant (γ_E), while the sweep and countergradient contributions remain unchanged throughout the unstable regime (Fig. 4b). This reflects the reorganization of coherent motions in the RSL into convective/thermal plumes that strengthen the positive coupling between vertical velocity (w') and temperature (T') fluctuations (Katul et al. 1997; Li and Bou-Zeid 2011). However, under stable conditions (Fig. 4b), γ_E and γ_S show opposite trends as z_d/L increases, such that they compensate for each other and therefore $|\gamma_{wT}|$ does not show a systematic dependence on z_d/L. In this respect, the contrast between momentum and heat transport efficiency as $|z_d/L|$ increases can be traced to a common origin (buoyancy modifying the transport by coherent structures), but acting through different mechanisms, namely that the reduced $|\gamma_{uw}|$ is associated with an increase in countergradient flux transport and weakening of downgradient fluxes (especially sweeps), while the enhanced $|\gamma_{wT}|$ under unstable conditions is largely due to more efficient heat transport by ejections within convective plumes.

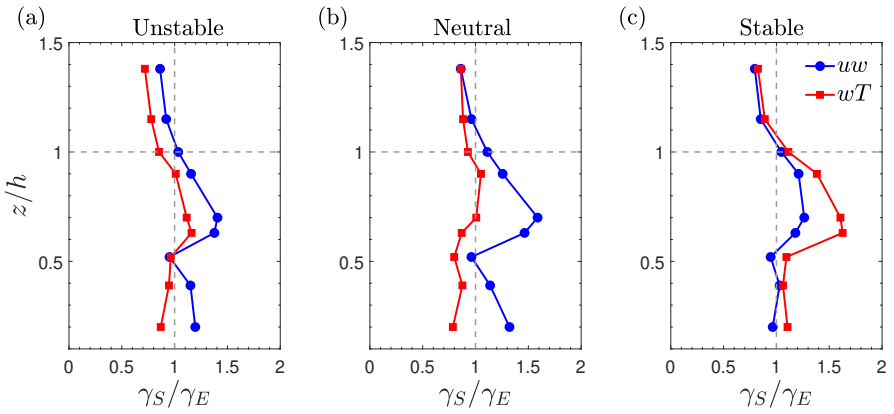


Fig. 5 Ensemble-average vertical profiles of the ratio of the correlation coefficients of sweeps (γ_S) to that of ejections (γ_E) for momentum and heat fluxes under (a) unstable, (b) near-neutral and (c) stable conditions.

The quadrant decomposition in Fig. 4 shows that ejections and sweeps dominate both $|\gamma_{uw}|$ and $|\gamma_{wT}|$ across the stability range in the RSL. Figure 5 further examines the relative contributions of these events through the vertical profiles of the sweep-to-ejection ratio γ_S/γ_E. Note that since both γ_S and γ_E are normalized by the same factor ($\sigma_u\sigma_w$ for the momentum flux and $\sigma_w\sigma_T$ for the heat flux; Eq. 4), the ratio becomes $\gamma_S/\gamma_E = F_S/F_E$, i.e., it is independent of the normalization by the standard deviations. For both fluxes and under the three stability classes, the ratio γ_S/γ_E exceeds unity in the upper part of the canopy and falls below unity in the RSL (Fig. 5a–c), consistent with the canonical transition from sweep-dominated transport near the canopy top to ejection-dominated transport further above in the RSL (Finnigan 2000; Poggi

et al. 2004). However, the dependence of this ratio on atmospheric stability differs between momentum and heat. For momentum, the ratio is largest under near-neutral conditions, reaching $\gamma_S/\gamma_E \approx 1.6$ at $z/h = 0.7$ (Fig. 5b), comparable to values reported for dense canopies (Poggi et al. 2004; Brunet 2020), and indicating a larger relative contribution of sweeps to momentum transport when buoyancy effects are weak. For heat, the ratio is largest under stable conditions, with $\gamma_S/\gamma_E \approx 1.6$ at $z/h = 0.6$ (Fig. 5c), and smallest under unstable conditions, where ejections dominate throughout the RSL (Fig. 5a). Under near-neutral conditions, γ_S/γ_E remains close to unity in the upper canopy, indicating comparable contributions from sweep and ejection events to heat transport (Fig. 5b).

This analysis of flux transport efficiencies and their decomposition into quadrant contributions provides a kinematic description of momentum–heat dissimilarity. To complement this analysis with a dynamic description, the following section examines the lagged cross-correlation functions of momentum and heat fluxes and their decorrelation timescales, and connects them to the pressure-driven flux destruction mechanisms in the respective flux budgets.

4.3 Lagged cross-correlations and flux decorrelation timescales

Figure 6 shows the ensemble-average cross-correlation functions of momentum (ρ_{uw}) and heat (ρ_{wT}) fluxes at $z/h = 1.38$, plotted against normalized time lag ($\tau u_*/h$) under the three atmospheric stability conditions. The upper axis shows the normalized spatial lag r/h, where $r = \tau\overline{U}$ is obtained using Taylor's hypothesis. In Fig. 6, ρ_{uw} remains near unity over a range of small lags ($r/h \lesssim 0.1$ under unstable and near-neutral conditions, and $r/h \lesssim 0.01$ under stable conditions) before decaying toward zero, indicating that small-scale eddies in the inertial subrange have negligible contribution to the net momentum flux. Conversely, ρ_{wT} deviates from unity at smaller lags under all three stability classes, suggesting that scales well within the inertial subrange ($r/h \ll 1$) maintain a w'-T' correlation and therefore participate in heat flux transport. Beyond this short lag behavior, both ρ_{uw} and ρ_{wT} decay to zero, giving an approximation of the decorrelation time/length scales of the largest eddies contributing to the respective fluxes. Under unstable conditions, this decorrelation occurs at $r \approx 10h$ for momentum and $r \approx 4h$ for heat (Fig. 6a). These scales become shorter under near-neutral conditions (Fig. 6b), and decrease further under stable conditions (Fig. 6c), where they become comparable to the canopy height ($r/h \approx 1$). Thus, the range of scales that transport the momentum flux is shifted toward larger eddies relative to that carrying the heat flux, at both its small-scale and large-scale limits. Momentum transport in the RSL is therefore accomplished by large, organized motions, whereas heat is transported across a narrower range of scales that extend into the inertial subrange.

The differences in these characteristic scales of momentum and heat flux carrying motions are further examined in Fig. 7, which compares the vertical

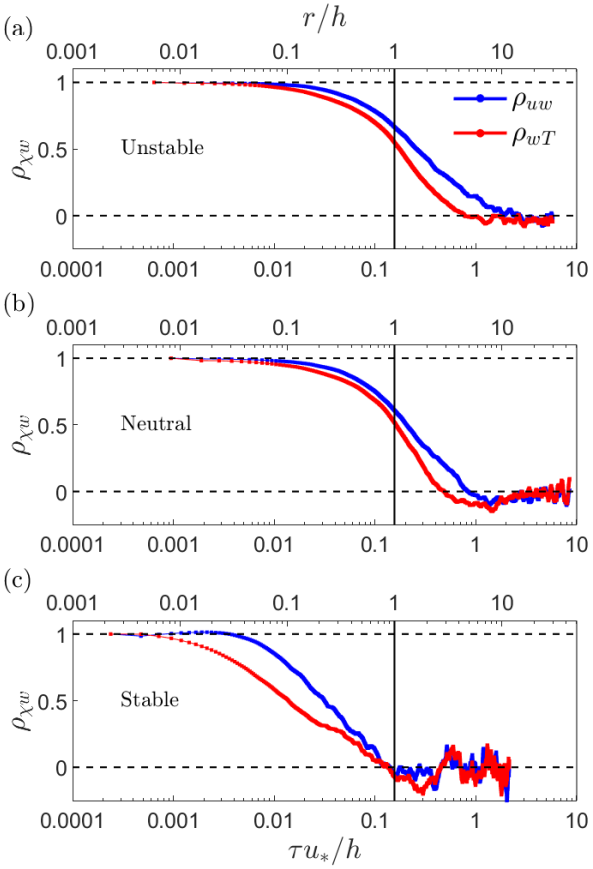


Fig. 6 Ensemble-average lagged cross-correlation functions of momentum and heat fluxes at $z/h = 1.38$ under (a) unstable, (b) near-neutral, and (c) stable conditions. The lower x-axis shows the normalized time lag, $\tau u_*/h$, while the upper x-axis shows the equivalent normalized spatial lag, r/h, where $r = \tau\overline{U}$ is obtained using Taylor's hypothesis. The vertical solid lines denote $r/h = 1$.

profiles of the decorrelation timescales (Eq. 6) of momentum ($\tau_{d(uw)}$) and heat ($\tau_{d(wT)}$) across the three stability classes. Under unstable and near-neutral conditions, both $\tau_{d(uw)}$ and $\tau_{d(wT)}$ remain relatively short in the lower canopy and increase with height, reaching their maximum values at $z/h = 1.38$ (Fig. 7a, b). However, $\tau_{d(uw)}$ consistently exceeds $\tau_{d(wT)}$ throughout the upper part of the canopy and in the RSL. Under stable conditions (Fig. 7c), both timescales are shorter than their counterpart under unstable and near-neutral conditions, and show no clear vertical trend, reflecting the inhibition of vertical turbulent exchange under stable stratification. The separation between $\tau_{d(uw)}$ and $\tau_{d(wT)}$ is also less pronounced under stable conditions. Although the cross-correlation functions reveal differences in the decorrelation rates of momentum and heat flux carrying motions, they still do not explain the mechanisms underlying

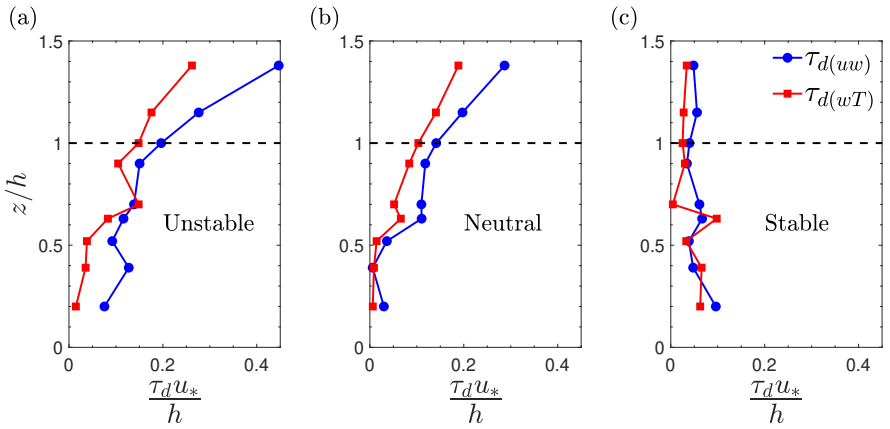


Fig. 7 Ensemble-average vertical profiles of normalized flux decorrelation timescales ($\frac{\tau_d u_*}{h}$) for momentum and heat fluxes under (a) unstable, (b) near-neutral, and (c) stable conditions.

this dissimilarity. We therefore examine the momentum and heat flux budgets in the following section (Section 4.4) to assess whether the difference between $\tau_{d(uw)}$ and $\tau_{d(wT)}$ is related to the differences in the efficiency of pressure-correlation terms in relaxing the respective fluxes.

4.4 Flux budgets and relaxation timescales

Figure 8 presents the normalized momentum and heat flux budgets across the RSL as a function of z_d/L, under the assumptions of stationary and horizontally homogeneous flow. The trends in the dominant terms of the $\overline{u'w'}$ (Fig. 8a) and $\overline{w'T'}$ (Fig. 8b) budgets broadly agree with those reported for the ASL in the Kansas experiment by Wyngaard et al. (1971), although the RSL budgets here exhibit greater scatter. A notable difference between the RSL and ASL is that the turbulent transport terms (T_{uw} and T_{wT}) are not negligible in the respective flux budgets (Figure 8), indicating that local production and destruction of the fluxes are not in balance and hence vertical transport redistributes them across the RSL. However, the mean gradient production terms (M_{uw} and M_{wT}) remain the dominant sources in both flux budgets (Fig. 8a, b) and are primarily balanced by the corresponding pressure-correlation terms (R_{uw} and R_{wT}). The buoyancy terms (B_{uw} and B_{wT}) exhibit stronger dependence on z_d/L, acting predominantly as sources under unstable conditions and sinks under stable conditions, so that under stable stratification their contributions complement those of the pressure terms in destroying the respective fluxes.

The budgets in Fig. 8 thus confirm that the pressure correlations are the dominant sink in both flux budgets, but the magnitudes of R_{uw} and R_{wT} alone are not an indication of the efficiency of pressure-scrambling in decorrelating

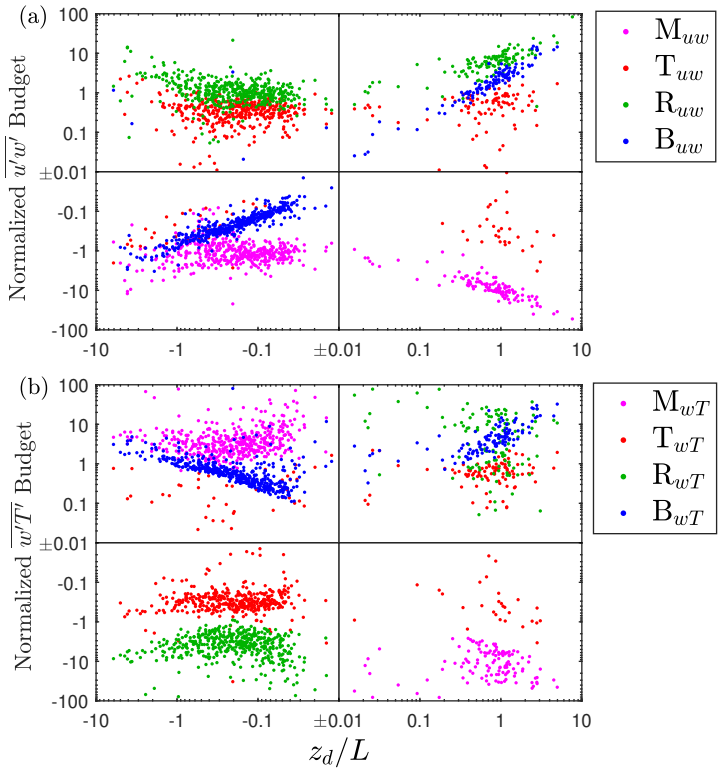


Fig. 8 (a) Momentum and (b) heat flux budgets in the RSL as a function of stability parameter z_d/L. Note that all terms in the $\overline{u'w'}$ and $\overline{w'T'}$ budgets are normalized by $\kappa z_d/u_*^3$ and $\kappa z_d/(u_*^2 T_*)$, respectively.

the momentum and heat fluxes. This efficiency is investigated here using the relaxation timescales estimated through the Rotta model (Eq. 8) to assess whether the difference between $\tau_{d(uw)}$ and $\tau_{d(wT)}$ in Fig. 7 can be traced to the pressure-scrambling mechanisms in the budgets.

The relaxation timescales of momentum (τ_{uw}) and heat (τ_{wT}) fluxes estimated from the Rotta closure (Eq. 8) are shown in Fig. 9. To assess the momentum-flux estimate, we compare it with the return-to-isotropy timescale τ_{TKE}, calculated as the ratio of turbulent kinetic energy (TKE) to its dissipation rate, ε (Pope 2001; Katul and Manes 2014). Here, ε is estimated from the second-order streamwise velocity structure function (D_{uu}) following Chamecki and Dias (2004), based on Kolmogorov's second similarity hypothesis in the inertial subrange (Kolmogorov 1941). Although obtained through a different approach, τ_{TKE} also represents the pressure-scrambling mechanism associated with the return of the Reynolds stress tensor toward isotropy (Pope 2001). Under unstable conditions, τ_{uw} and τ_{TKE} agree closely (Fig. 9), providing support for the Rotta-based estimation from the momentum-flux budget and for the

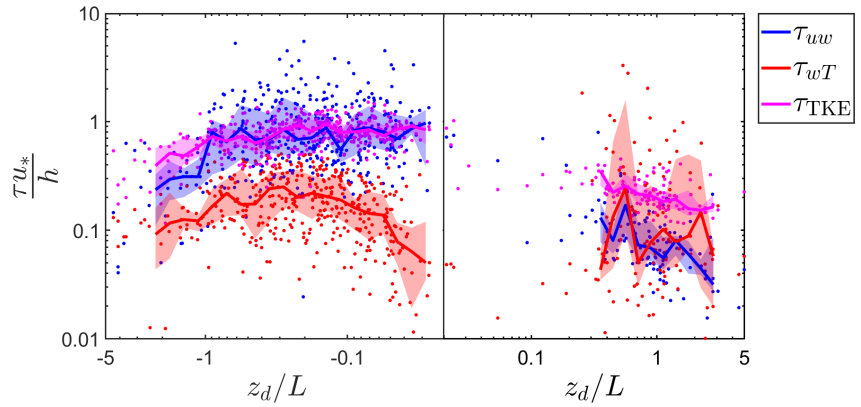


Fig. 9 Normalized relaxation time scales for momentum (τ_{uw}) and heat (τ_{wT}) fluxes estimated from the Rotta model as a function of the stability parameter (z_d/L) in the RSL. Solid curves indicate the median, shaded regions represent the inter-quartile range, and dots show individual data points.

value of C_1 adopted here. Under stable conditions, however, the substantially larger scatter limits a robust comparison between the two approaches.

The relaxation timescales also differ between momentum and heat fluxes across the RSL, with τ_{uw} generally exceeding τ_{wT}, particularly under near-neutral and unstable conditions. This behavior is consistent with the decorrelation timescales discussed in Fig. 7, where $\tau_{d(uw)}$ exceeded $\tau_{d(wT)}$ throughout the RSL. The similarity in the behavior of these timescales indicates a potential link between the pressure-driven relaxation of fluxes in the flux budgets, and the decorrelation timescales obtained from the cross-correlation functions.

To examine this latter link, Fig. 10 compares the relaxation and decorrelation timescales for each flux across the three stability regimes. For the momentum flux, the two timescales exhibit an approximately linear relationship and lie close to the 1:1 reference line, although τ_{uw} is generally larger than $\tau_{d(uw)}$. For heat, a comparable relationship holds under unstable conditions only, whereas near-neutral and stable conditions exhibit considerably greater scatter (Fig. 10b), consistent with weak heat fluxes under neutral conditions and the smaller number of data blocks satisfying the budget quality control under stable stratification. Overall, the correspondence between τ and τ_d in Fig. 10 links the pressure-related terms governing flux relaxation to the observed decorrelation behavior of momentum and heat fluxes. These results provide a dynamical perspective on momentum–heat transport dissimilarity by connecting the lifetime of the flux carrying eddies to the pressure-scrambling mechanisms represented in their respective flux budgets.

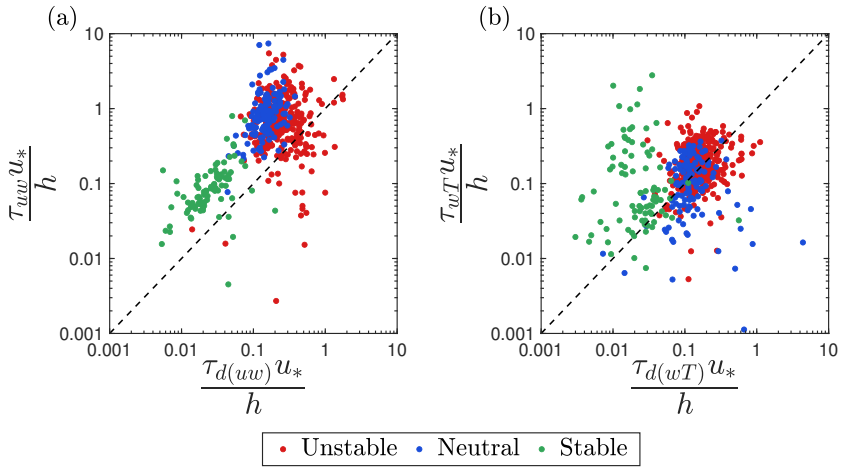


Fig. 10 Comparison between relaxation (τ) and decorrelation (τ_d) timescales within the RSL under unstable, near-neutral, and stable conditions for (a) momentum flux and (b) heat flux. The black dashed line indicates the 1:1 relationship.

5 Conclusions

Momentum and heat transport in the vegetation RSL exhibit contrasting responses to atmospheric stability, and apart from some analogies to surface layer turbulence, the mechanisms underlying their dissimilarity remain less studied in the RSL. The work here investigated these mechanisms above a tall and dense forest canopy using eddy-covariance observations spanning unstable, near-neutral, and stable stratification. The analysis of flux transport efficiencies, quadrant decomposition, lagged cross-correlations, and steady-state flux budgets characterized the kinematic aspects of this dissimilarity governed by coherent structures in the RSL, as well as the dynamical mechanisms responsible for the contrasting timescales governing momentum and heat transport.

Under near-neutral conditions, momentum transport efficiency in the RSL ($|\gamma_{uw}| \approx 0.5$) is consistently higher than MOST predictions for the ASL, whereas the heat transport efficiency ($|\gamma_{wT}| \approx 0.2$) is lower, indicating that the common assumption of momentum–heat similarity under neutral conditions is not evident in the RSL. The reduced transport efficiency of momentum with increasing $|z_d/L|$ is attributed to a simultaneous weakening of downgradient fluxes (predominantly sweeps) and strengthening of countergradient fluxes (inward and outward interactions) under both unstable and stable conditions, suggesting that the presence of buoyancy, regardless of its sign, disrupts the efficient momentum transport organized by the canonical canopy-top ejection–sweep cycle. In contrast, the enhanced transport efficiency of heat under unstable conditions is driven almost entirely by the increased contribution of the ejection quadrant within buoyant plumes, while the sweep and countergradient contributions remain largely invariant with z_d/L. Under stable stratification,

the heat transport efficiency shows no systematic dependence on z_d/L in the RSL, a feature traced here to the opposing trends of the ejection and sweep contributions with z_d/L, which compensate for each other such that the net correlation coefficient remains nearly unchanged.

The analysis of lagged cross-correlations indicates that the momentum flux is transported over a range of eddy scales that is shifted toward larger motions compared to the heat flux. Specifically, small-scale eddies within the inertial subrange have negligible contribution to net momentum transport, but maintain an active w'-T' coupling and hence participate in heat transport across all stability regimes. In this respect, momentum exchange is limited to larger, more organized motions while heat transport extends into inertial scales, such that momentum-carrying eddies exhibit consistently longer decorrelation timescales (longer lifetimes) than heat-carrying eddies throughout the RSL. The analysis of the steady-state flux budgets demonstrates that this contrast in eddy lifetimes has a dynamical origin in the pressure-scrambling mechanisms that act as the primary sink for both fluxes. The close correspondence between the kinematic decorrelation timescales and the Rotta relaxation timescales derived from the budget closure confirms that pressure–temperature-gradient interactions destroy heat flux covariance more rapidly than pressure–strain interactions destroy momentum flux.

Collectively, these findings link the departure from the Reynolds analogy in the vegetation RSL to both the buoyancy-driven reorganization of coherent motions and the different efficiency of pressure-scrambling processes, both of which have direct implications for canopy turbulence parameterization (Bonan et al. 2018; Li 2019). In the context of first-order closure modeling, the momentum–heat dissimilarity observed here even under near-neutral conditions, along with the contrasting stability dependence of sweeps and ejections, challenges the conventional assumption of a constant or unity turbulent Prandtl number in near-neutral and stable RSL flows. For second-order and cospectral closure models (Katul and Albertson 1998; Cava et al. 2006; Katul and Manes 2014; Mortarini et al. 2025), the non-negligible role of vertical turbulent transport in the RSL flux budgets underscores that local equilibrium between mean-gradient production and pressure destruction does not strictly hold above tall canopies. More importantly, while the momentum relaxation timescale closely follows the TKE-based return-to-isotropy timescale under unstable conditions, the systematically shorter relaxation timescale for heat implies that parameterizing slow pressure redistribution for momentum and scalars using a single master dissipation timescale and identical Rotta constants is insufficient to capture the faster destruction of scalar fluxes in the RSL.

Acknowledgements K. Ghannam acknowledges support from the Northeastern University Provost Office through a TIER 1 grant. The GoAmazon 2014/5 field study was supported by the U.S. Department of Energy (grant SC0011075) and benefited from logistic support provided by the Large-scale Biosphere-Atmosphere Experiment in Amazonia (LBA). The authors thank Tobias Gerken for making the GoAmazon tower data available to them.

Statements and Declarations

Competing interests. The authors declare no competing interests.

Data availability. The eddy-covariance data used in this study were collected during the GoAmazon field campaign at the Cuieiras Biological Reserve (Fuentes et al. 2016) and were provided to the authors by the campaign investigators. The processed data needed to reproduce the figures are available from the corresponding author upon reasonable request.

Author contributions. K.G. conceived the study and supervised the work. S.T. performed the data analysis and prepared the figures. Both authors wrote and reviewed the manuscript.

References

Andrén A, Moeng CH (1993) Single-point closures in a neutrally stratified boundary layer. Journal of Atmospheric Sciences 50(20):3366–3379

Banerjee T, Li D, Juang JY, Katul G (2016) A spectral budget model for the longitudinal turbulent velocity in the stable atmospheric surface layer. Journal of the Atmospheric Sciences 73(1):145–166

Bonan GB, Patton EG, Harman IN, Oleson KW, Finnigan JJ, Lu Y, Burakowski EA (2018) Modeling canopy-induced turbulence in the earth system: A unified parameterization of turbulent exchange within plant canopies and the roughness sublayer (clm-ml v0). Geoscientific Model Development 11(4):1467–1496

Brunet Y (2020) Turbulent flow in plant canopies: historical perspective and overview. Boundary-Layer Meteorology 177(2):315–364

Cava D, Katul G (2012) On the scaling laws of the velocity-scalar cospectra in the canopy sublayer above tall forests. Boundary-layer meteorology 145(2):351–367

Cava D, Katul G, Scrimieri A, Poggi D, Cescatti A, Giostra U (2006) Buoyancy and the sensible heat flux budget within dense canopies. Boundary-layer meteorology 118(1):217–240

Chamecki M, Dias N (2004) The local isotropy hypothesis and the turbulent kinetic energy dissipation rate in the atmospheric surface layer. Quarterly Journal of the Royal Meteorological Society: A journal of the atmospheric sciences, applied meteorology and physical oceanography 130(603):2733–2752

Choi T, Hong J, Kim J, Lee H, Asanuma J, Ishikawa H, Tsukamoto O, Zhiqiu G, Ma Y, Ueno K, et al. (2004) Turbulent exchange of heat, water vapor, and momentum over a tibetan prairie by eddy covariance and flux variance measurements. Journal of Geophysical Research: Atmospheres 109(D21)

Chowdhuri S, Prabha TV (2019) An evaluation of the dissimilarity in heat and momentum transport through quadrant analysis for an unstable atmospheric surface layer flow. Environmental Fluid Mechanics 19(2):513–542

Chowdhuri S, Ghannam K, Banerjee T (2022) A scale-wise analysis of intermittent momentum transport in dense canopy flows. Journal of Fluid Mechanics 942:A51

Christen A, van Gorsel E, Vogt R (2007) Coherent structures in urban roughness sublayer turbulence. International journal of Climatology 27(14):1955–1968

De Bruin H, Kohsiek W, Van Den Hurk B (1993) A verification of some methods to determine the fluxes of momentum, sensible heat, and water vapour using standard deviation and structure parameter of scalar meteorological quantities. Boundary-Layer Meteorology 63(3):231–257

Dupont S, Patton EG (2012a) Influence of stability and seasonal canopy changes on micrometeorology within and above an orchard canopy: The chats experiment. Agricultural and forest meteorology 157:11–29

Dupont S, Patton EG (2012b) Momentum and scalar transport within a vegetation canopy following atmospheric stability and seasonal canopy changes: the chats experiment. Atmospheric Chemistry and Physics 12(13):5913–5935

Finnigan J (2000) Turbulence in plant canopies. Annual review of fluid mechanics 32(1):519–571

Finnigan JJ, Shaw RH, Patton EG (2009) Turbulence structure above a vegetation canopy. Journal of Fluid Mechanics 637:387–424

Freire L, Gerken T, Ruiz-Plancarte J, Wei D, Fuentes J, Katul G, Dias N, Acevedo O, Chamecki M (2017) Turbulent mixing and removal of ozone within an amazon rainforest canopy. Journal of Geophysical Research: Atmospheres 122(5):2791–2811

Fuentes JD, Chamecki M, Nascimento dos Santos RM, Von Randow C, Stoy PC, Katul G, Fitzjarrald D, Manzi A, Gerken T, Trowbridge A, et al. (2016) Linking meteorology, turbulence, and air chemistry in the amazon rain forest. Bulletin of the American Meteorological Society 97(12):2329–2342

Gerken T, Ruddell BL, Fuentes JD, Araújo A, Brunsell NA, Maia J, Manzi A, Mercer J, dos Santos RN, Von Randow C, et al. (2018) Investigating the mechanisms responsible for the lack of surface energy balance closure in a central amazonian tropical rainforest. Agricultural and Forest Meteorology 255:92–103

Ghannam K, Duman T, Salesky ST, Chamecki M, Katul G (2017) The nonlocal character of turbulence asymmetry in the convective atmospheric boundary layer. Quarterly Journal of the Royal Meteorological Society 143(702):494–507

Ghannam K, Katul GG, Bou-Zeid E, Gerken T, Chamecki M (2018) Scaling and similarity of the anisotropic coherent eddies in near-surface atmospheric turbulence. Journal of the atmospheric sciences 75(3):943–964

Ghannam K, Poggi D, Bou-Zeid E, Katul GG (2020) Inverse cascade evidenced by information entropy of passive scalars in submerged canopy flows. Geophysical Research Letters 47(9):e2020GL087,486

Harman IN, Finnigan JJ (2007) A simple unified theory for flow in the canopy and roughness sublayer. Boundary-layer meteorology 123(2):339–363

Kaimal JC, Finnigan JJ (1994) Atmospheric boundary layer flows: their structure and measurement. Oxford university press
Katul G, Albertson JD (1998) An investigation of higher-order closure models for a forested canopy. Boundary-Layer Meteorology 89(1):47–74
Katul G, Kuhn G, Schieldge J, Hsieh CI (1997) The ejection-sweep character of scalar fluxes in the unstable surface layer. Boundary-Layer Meteorology 83(1):1–26
Katul G, Poggi D, Cava D, Finnigan J (2006) The relative importance of ejections and sweeps to momentum transfer in the atmospheric boundary layer. Boundary-layer meteorology 120(3):367–375
Katul GG, Manes C (2014) Cospectral budget of turbulence explains the bulk properties of smooth pipe flow. Physical Review E 90(6):063,008
Katul GG, Parlange MB (1994) On the active role of temperature in surface-layer turbulence. Journal of Atmospheric Sciences 51(15):2181–2195
Kolmogorov AN (1941) The local structure of turbulence in incompressible viscous fluid for very large reynolds. Numbers In Dokl Akad Nauk SSSR 30:301
Lan C, Wang B, Zheng D, Wang Y, Zhang Z, Fang R (2022) Decreased dissimilarity of turbulent transport attributed to large eddies. Quarterly Journal of the Royal Meteorological Society 148(744):1262–1279
Launiainen S, Vesala T, Mölder M, Mammarella I, Smolander S, Rannik Ü, Kolari P, Hari P, Lindroth A, G Katul G (2007) Vertical variability and effect of stability on turbulence characteristics down to the floor of a pine forest. Tellus B: Chemical and Physical Meteorology 59(5):919–936
Li D (2019) Turbulent prandtl number in the atmospheric boundary layer–where are we now? Atmospheric Research 216:86–105
Li D, Bou-Zeid E (2011) Coherent structures and the dissimilarity of turbulent transport of momentum and scalars in the unstable atmospheric surface layer. Boundary-Layer Meteorology 140(2):243–262
Macdonald R (2000) Modelling the mean velocity profile in the urban canopy layer. Boundary-Layer Meteorology 97(1):25–45
Mironov DV (2001) Pressure-potential-temperature covariance in convection with rotation. Quarterly Journal of the Royal Meteorological Society 127(571):89–110
Moeng CH, Wyngaard JC (1986) An analysis of closures for pressure-scalar covariances in the convective boundary layer. Journal of Atmospheric Sciences 43(21):2499–2513
Mölder M, Klemedtsson L, Lindroth A (2004) Turbulence characteristics and dispersion in a forest—tests of thomson's random-flight model. Agricultural and forest meteorology 127(3-4):203–222
Mortarini L, Katul G, Mauricio Cely-Toro I, Quaresma Dias-Júnior C, Mammarella I (2025) The role of thermal stratification on the co-spectral properties of momentum transport above an amazonian forest. Quarterly Journal of the Royal Meteorological Society p e5024
Patton EG, Sullivan PP, Shaw RH, Finnigan JJ, Weil JC (2016) Atmospheric stability influences on coupled boundary layer and canopy turbulence. Jour-

nal of the Atmospheric Sciences 73(4):1621–1647
Poggi D, Katul G (2007) The ejection-sweep cycle over bare and forested gentle hills: a laboratory experiment. Boundary-layer meteorology 122(3):493–515
Poggi D, Porporato A, Ridolfi L, Albertson J, Katul G (2004) The effect of vegetation density on canopy sub-layer turbulence. Boundary-Layer Meteorology 111(3):565–587
Pope SB (2001) Turbulent flows. Measurement Science and Technology 12(11):2020–2021
Raupach M (1981) Conditional statistics of reynolds stress in rough-wall and smooth-wall turbulent boundary layers. Journal of Fluid Mechanics 108:363–382
Raupach MR, Finnigan JJ, Brunei Y (1996) Coherent eddies and turbulence in vegetation canopies: the mixing-layer analogy. Boundary-layer meteorology 78(3):351–382
Shaw RH, Tavangar J, Ward DP (1983) Structure of the reynolds stress in a canopy layer. Journal of Applied Meteorology and Climatology 22(11):1922–1931
Starkenburg D, Metzger S, Fochesatto GJ, Alfieri JG, Gens R, Prakash A, Cristóbal J (2016) Assessment of despiking methods for turbulence data in micrometeorology. Journal of Atmospheric and Oceanic Technology 33(9):2001–2013
Stull RB (2012) An introduction to boundary layer meteorology, vol 13. Springer Science & Business Media
Torkelson G, Price TA, Stoll R (2022) Momentum and turbulent transport in sparse, organized vegetative canopies. Boundary-Layer Meteorology 184(1):1–24
Vickers D, Mahrt L (1997) Quality control and flux sampling problems for tower and aircraft data. Journal of atmospheric and oceanic technology 14(3):512–526
Wilczak J (1984) Large-scale eddies in the unstably stratified atmospheric surface layer. part i: Velocity and temperature structure. Journal of Atmospheric Sciences 41(24):3537–3550
Wyngaard J, Coté O, Izumi Y (1971) Local free convection, similarity, and the budgets of shear stress and heat flux. Journal of Atmospheric Sciences 28(7):1171–1182
Wyngaard JC, Moeng CH (1992) Parameterizing turbulent diffusion through the joint probability density. Boundary-layer meteorology 60(1):1–13
Zahn E, Bou-Zeid E, Good SP, Katul GG, Thomas CK, Ghannam K, Smith JA, Chamecki M, Dias NL, Fuentes JD, et al. (2022) Direct partitioning of eddy-covariance water and carbon dioxide fluxes into ground and plant components. Agricultural and Forest Meteorology 315:108,790